applied sciences

MDPI

Article

Trial of FastEddy Simulation of Building-Induced Airflow and the Comparison with LIDAR and Flight Data in an Operating Airport

Kai Kwong Lai, Man Lok Chong and Pak Wai Chan *

Hong Kong Observatory, Hong Kong, China; mlchong@hko.gov.hk (M.L.C.)
* Correspondence: pwchan@hko.gov.hk

Abstract

The performance of FastEddy, a GPU-based large eddy simulation model, in simulating building-induced turbulent flow in an operating airport is studied for the first time through four examples, including a super typhoon case at Hong Kong International Airport (HKIA) and a real case of low-level wind effect. The simulation results are quantitatively compared with wind observations from Light Detection and Ranging (LIDAR) systems for selected cases, and with aircraft data and pilot reports in one example of low-level wind effect. The FastEddy model is found to perform reasonably well through these case studies, even for the radial component of the winds exceeding 20 m/s in a highly turbulent airflow simulation of a typhoon, as well as turbulent airflow features in a building complex at and around HKIA. The building-induced turbulent flow as observed by the LIDARs and the aircraft are largely reproduced. The scatter plots of the model-simulated and the observed Doppler velocities have good correlation in terms of the slope of the best-fit linear equation, correlation coefficient and root-mean-square difference. Moreover, for the case of low-level wind effect, FastEddy simulation is found to provide useful insight into the turbulent flow arising from the new terminal building over the northeastern part of HKIA (near 22.325° N 113.918° E) under construction. Further research directions for studying the performance of FastEddy are also discussed, such as considering more complex urban environments, comparison with in situ measurements of anemometers, and direct output of the eddy dissipation rate (EDR) from the model for comparing with LIDAR and anemometer-based measurements.

Keywords: FastEddy; LIDAR; flight data

Check for updates

Academic Editor: Min-Suk Bae

Received: 4 May 2026
Revised: 12 June 2026
Accepted: 19 June 2026
Published: 25 June 2026

Copyright: © 2026 by the authors. Licensee MDPI, Basel, Switzerland. This article is an open access article distributed under the terms and conditions of the Creative Commons Attribution (CC BY) license.

1. Introduction

Apart from terrain-induced airflow disturbances, airflow disruption by human-made structures, also known as low-level wind effect, is gaining more attention for airports, including in Hong Kong [1] and around the world [2,3]. Recent LES studies have also characterized terrain-induced turbulence for air safety considerations in airport siting [4], underscoring the importance of high-resolution modeling approaches in complex environments. Such airflow disruption over the runway could pose a safety risk to aircraft landing and taking off. Due to the sustainable development of operating airports, especially for those built on reclaimed land, more structures could be constructed adjacent to the runways and the glide paths, such as exhibition halls, shopping plazas, hotels and cargo terminals. Under favorable meteorological conditions, airflow disturbances arising from these human-made structures may be felt by the pilots of the arriving aircraft, mostly in the form of

"buffeting" which may roughly correspond to low-level moderate turbulence. At HKIA, the Hong Kong Observatory operates a state-of-the-art Windshear and Turbulence Warning System that integrates multiple real-time sensors, including a Terminal Doppler Weather Radar (TDWR) system, four long-range Doppler LIDARs, eight short-range LIDARs, wind profilers, weather buoys, and a dense network of surface stations. These systems feed into an in-house algorithm that generates real-time alerts, relayed to aircraft via ATIS and air traffic control. Importantly, no LES models are currently used operationally at HKIA. Forecasting of turbulence zones relies on empirical detection and pilot reports rather than predictive numerical modeling. For Hong Kong International Airport (HKIA), any new structures to be set up inside and around the airport have to go through a low-level wind study before obtaining approval for construction, following the criterion adopted in the Netherlands [5]. For any structures that have already been set up, low-level turbulence is monitored using short-range Light Detection and Ranging (LIDAR) systems (abbreviated as SRLs). The observed features of low-level turbulent flow may also be studied using the coupling of meso-scale meteorological model and computation fluid dynamics (CFD) model [6], or even more specifically the Regional Atmospheric Modelling System (RAMS) and/or Parallelized Large Eddy Simulation (LES) model (PALM), in hypothetical [7] and operational airports [8].

While RAMS coupled with PALM is found to reproduce many features of building-induced turbulence at HKIA, the computational cost is extensive and it is mostly run on a CPU. In recent years, a GPU version of the LES model for studying turbulence and fine-scale atmospheric processes, FastEddy [9], has been made available, with a faster prediction rate and less computational resources required. The FastEddy model is configured to simulate airflows under microscale features such as buildings [10] and terrain [11]; a case study was also performed using FastEddy to simulate the impact of a lake breeze front passage over Salt Lake City, Utah, across an urban environment [12]. However, it is noted that the model does not explicitly solve for atmosphere radiation effects [12], and under its generalized actuator disk (GAD) model for wind energy research, there is higher turbulence variability under stable conditions [13]. To highlight the practical advantage of GPU acceleration, we include a table comparing computation time to physical time for our HKIA case studies, along with comparative runtimes for RAMS+PALM.

This paper serves as the first attempt to test the capability of FastEddy in simulating building-induced airflow features at HKIA. The novelty lies not in replacing existing systems, but in demonstrating that GPU-accelerated LES can enable near real-time simulations at airport scale, which was previously infeasible with CPU-based models such as RAMS+PALM.

In particular, the novelty of the application lies in comparing the FastEddy simulation results with the observations from SRLs in different kinds of weather conditions, including the typhoon case of Ragasa in 2025, which has not been reported in the literature before. The model-simulated wind and turbulence are compared with the actual LIDAR observations for selected cases. As it is a preliminary result, FastEddy has not yet been configured to output eddy dissipation rate (EDR), so that only the turbulent kinetic energy (TKE) output from the model is compared with the EDR map based on LIDAR systems following the calculation method of [14]. Moreover, an actual case of low-level wind effect is reported in this paper, with turbulence associated with a new terminal building at HKIA under the rather rare situation of a strong northwesterly wind on an arriving aircraft, through comparison of FastEddy simulation results with SRL observations and flight data recorded on the aircraft. This paper serves as a first step to study the performance of FastEddy in an operating airport. More detailed comparison results, such as the simulation capability

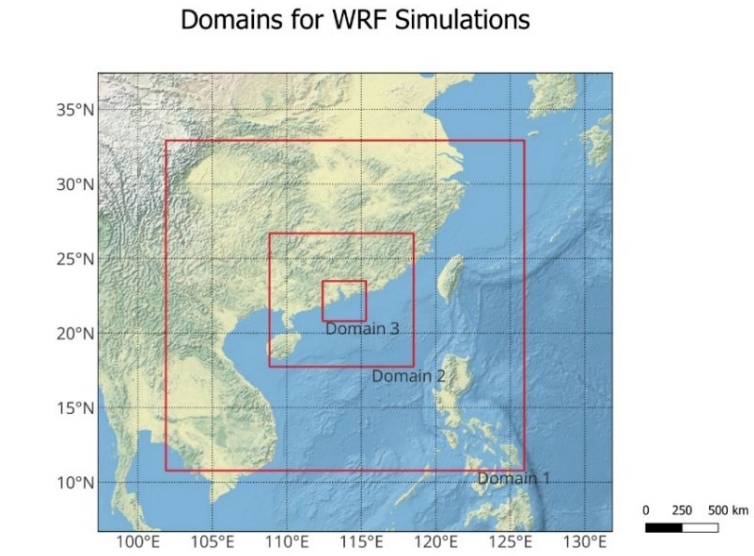
of mean winds and gusts at the locations of the ground-based anemometers, will be the subject of further studies.

2. Setup of the Model

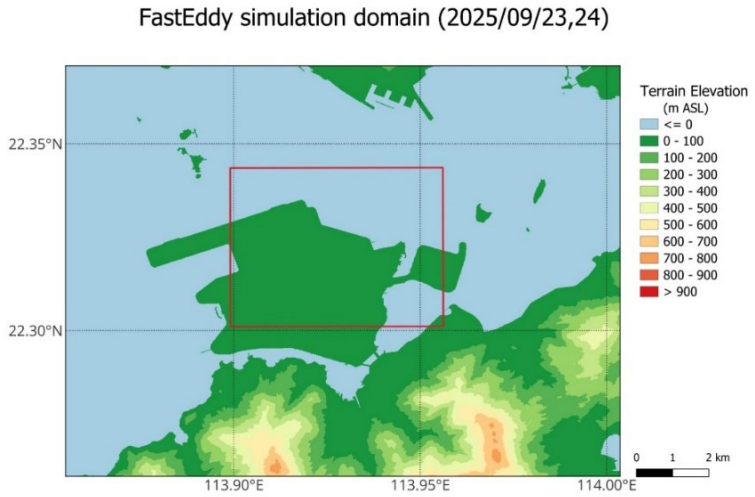
FastEddy version 4.0.1 (homepage: https://fasteddy.colorado.edu, source code repository: https://github.com/NCAR/FastEddy-model, accessed on 23 April 2026. documentation: https://fasteddy-model.readthedocs.io/en/latest/, accessed on 23 April 2026) is a LES model used to study turbulence and fine-scale atmospheric processes in the boundary layer. Recent GPU-accelerated atmospheric models, such as LEX [15] and DP-SCREAMv1 [16], highlight the broader trend toward high-performance LES frameworks. To situate FastEddy within this emerging landscape, Table 1 compares its runtime performance with the CPU-based PALM model under similar domain configurations. FastEddy required 104,100 s of wall-clock runtime to simulate 10,800 s of physical time using a single GPU, while PALM required 61,255 s to simulate 36,000 s of physical time using 1000 processors. Despite the longer wall-clock runtime, FastEddy achieved a substantially lower normalized cost (1.44×10^{-6} s per simulated second per grid point per processor) compared with PALM (1.77×10^{-5}). This efficiency gain highlights the advantage of GPU acceleration, enabling near real-time LES simulations with much less computational resources. In these simulations, the domain is set over HKIA, with boundary conditions provided by Weather Research and Forecasting (WRF) model version 4.5.2 at 1 km horizontal resolution. WRF is run in three grids (with the domains shown in Figure 1a), with horizontal resolutions of 25 km, 5 km and 1 km. Grid 3 is then nested with FastEddy. Two sample domains of FastEddy inside and around HKIA are shown in Figure 1b,c. The computational grids have a horizontal resolution of 15 meters and a vertical resolution of 67 meters, with a vertical deformation factor of 0.42 applied to better represent the atmosphere. The vertical deformation factor controls how grid spacing varies with altitude: a value of 0 corresponds to uniform spacing, while 1.0 produces the strongest compression near the surface. With the current setting of 0.42, the vertical grid spacing ranges from about 28 m near the surface to 142.7 m aloft (for points without terrain), ensuring fine resolution close to the ground while reducing computational cost at higher levels, as depicted in Figure 1d. Each run uses a time step of 0.03125 s with the RK3 WS2002 scheme [17]. Turbulence is represented by the Lilly/Smagorinsky method [13], with prognostic turbulent kinetic energy (TKE) included, and moisture processes such as condensation and microphysics are active. The surface layer is parameterized with roughness lengths and offshore options, while explicit filters and stability dependent base state fields are also configured. These settings together make the simulations stable and able to capture realistic atmospheric dynamics. A summary table of the parameterization settings is included in Appendix A.

Table 1. Runtime comparison of FastEddy and PALM illustrating GPU acceleration efficiency.

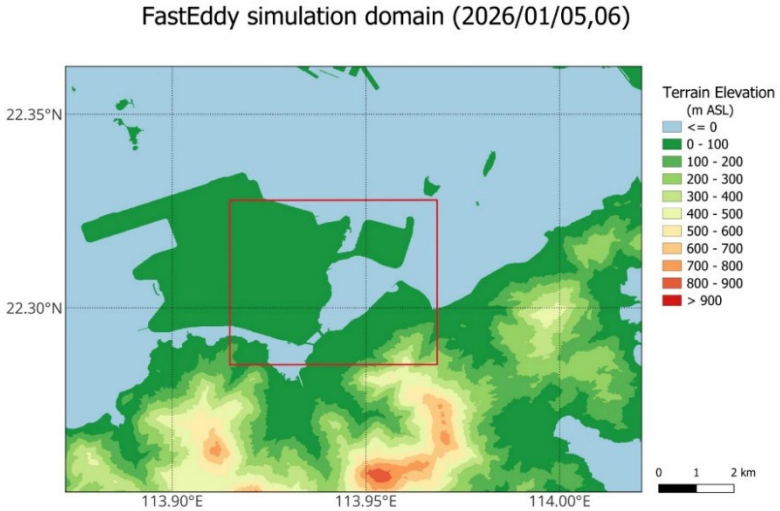
Model	Runtime (s)	Physical Time Simulated (s)	Processors/GPUs Used	Domain Size	Total Grid Points (nx × ny × nz)	Runtime (s) per Simulated Second per Grid Point per Processor
PALM	61,255	36,000	1000	1000 × 800 × 120	96,000,000	1.77242×10^{-5}
FastEddy	104,100	10,800	1	368 × 314 × 58	6,702,016	1.43821×10^{-6}



(**a**)

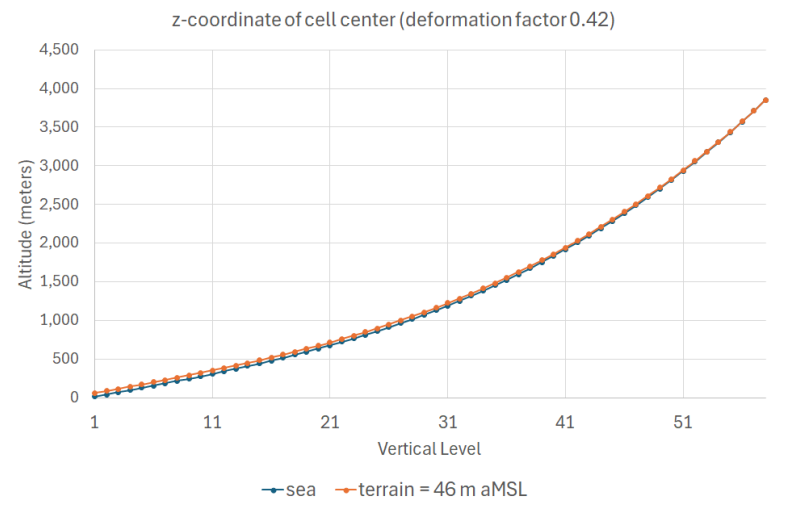


(**b**)



(**c**)

Figure 1. *Cont*.



(**d**)

Figure 1. Domains of WRF model grids (**a**) and domains of FastEddy for two cases (**b**,**c**), with red boxes outlining the simulated regions. Vertical grid spacing profiles of the simulation with deformation factor 0.42 (**d**).

The initial conditions are prepared from several data sources to ensure more realistic representation of the state of the atmosphere. Terrain roughness is derived from land use data provided by The WorldCover 2021 Map v200 [18]. Digital elevation data (DEM) are taken from the DTM dataset of Hong Kong Special Administrative Region (HKSAR) open data, which provides accurate ground elevation. Building structures are incorporated using 3D Spatial Data 3D BIT00 from the Common Spatial Data Infrastructure Portal, so the model can account for urban effects. For the atmospheric background, ERA5 reanalysis data from the European Centre for Medium Range Weather Forecast (ECMWF) is used to generate initial conditions for the WRF simulations, which then provide boundary conditions to FastEddy. This combination of global reanalysis, regional WRF simulation, and local terrain and building data ensures the simulations start from a physically consistent and realistic state.

The comparison between model output and observation data follows a systematic method. For each model data record, observation records within 5 min time differences are identified. Then, the time distance and spatial distance in east, north, and upstream directions between the model record and observation records are calculated. Finally, the observation record with the minimum time distance and spatial distance is selected. This method ensures that each model output is matched with the closest possible observation in both time and space. The results showed that the simulation records matched the observation records within 5 min, with minimized spatial and temporal differences.

3. Airflow Disturbances in a Building Complex

Many cases presented in this paper are taken from [19]. To recap, under north to northwesterly winds, airflow disturbances appear when the wind blows over the building complex in the southern part of the airport island of HKIA (Figure 2a—comparing the rather disturbed flow to the west of the SRL at Hong Kong Boundary Crossing Facility (HKBCF) with the rather uniform flow to the east of this LIDAR). However, the RAMS-PALM coupled model does not show the same degree of airflow disturbances even with incorporation of the buildings inside and to the south of the runways (Figure 2b).

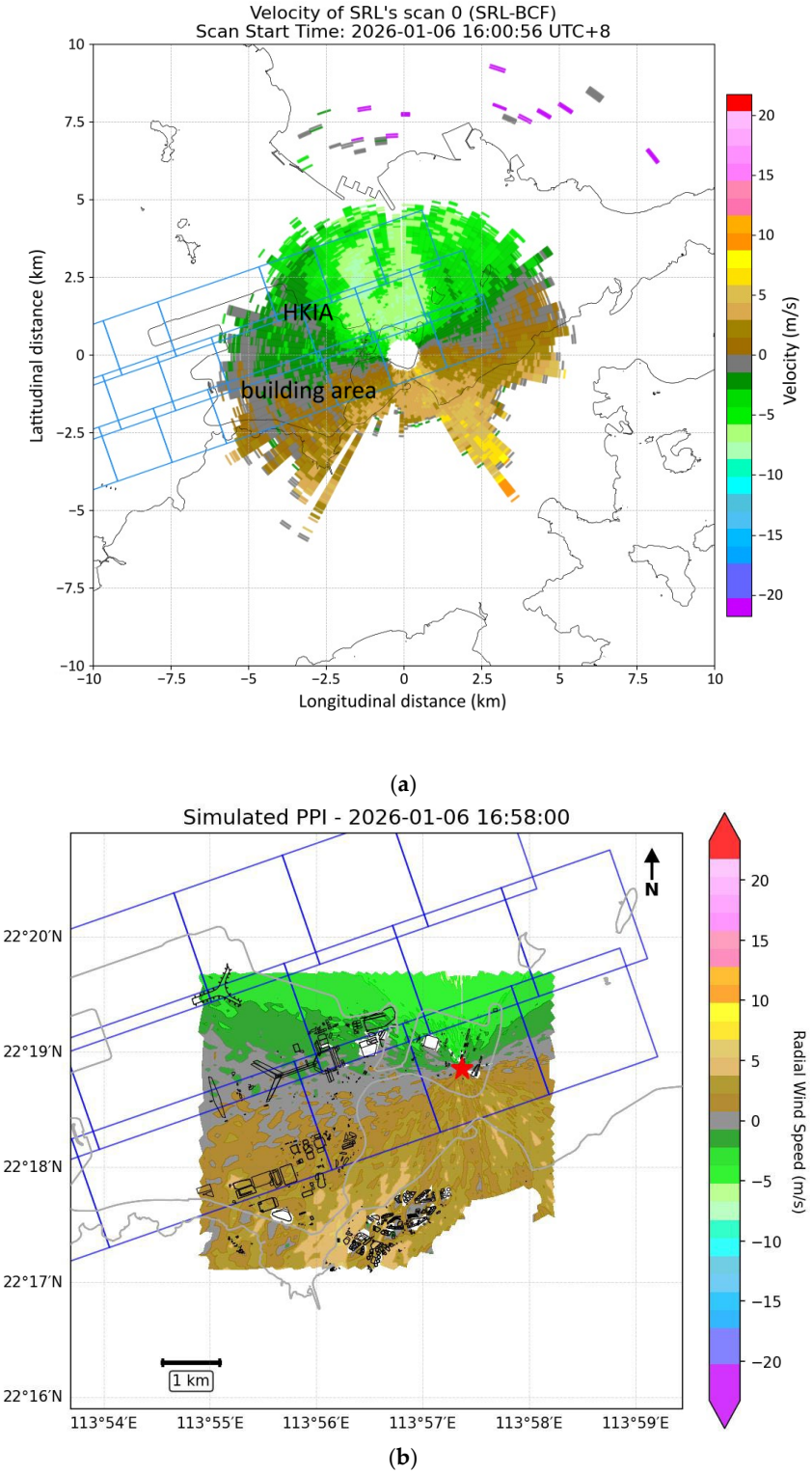
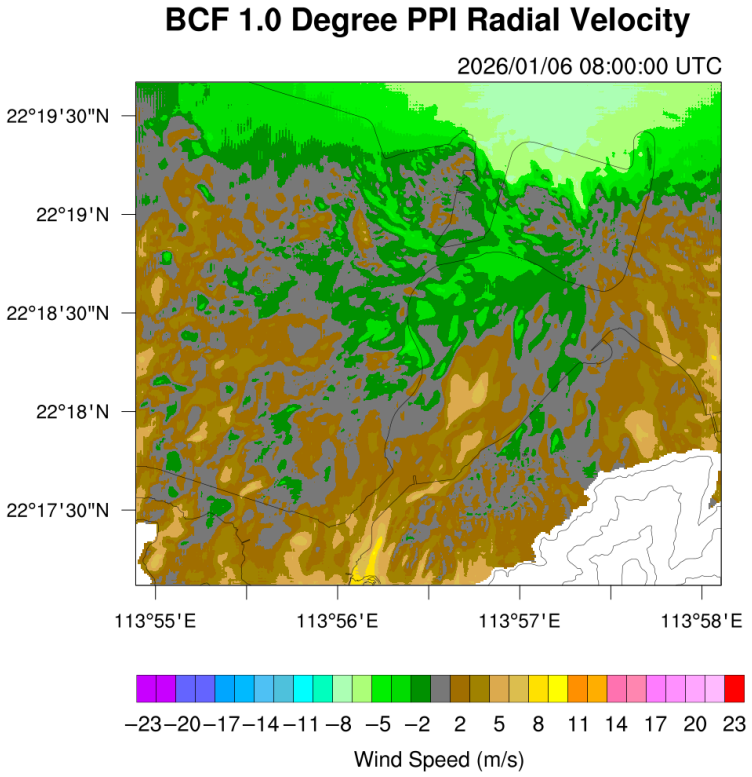


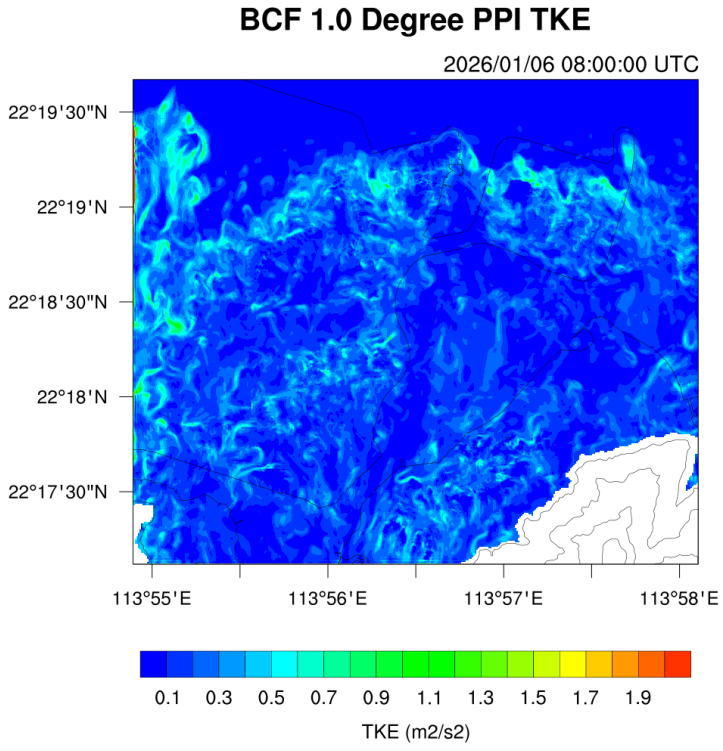
Figure 2. SRL PPI 1.0 degree Doppler velocity imagery (**a**) and RAMS-PALM simulation result (**b**), with the red star in (**b**) denoting the SRL location.

WRF-FastEddy simulation is performed starting at 05 UTC on 6 January 2026. It takes some time in the simulation for the turbulence to develop, such that the building-induced turbulence should be fully developed after about 2 h of simulation time, i.e., 08 UTC on 6 January 2026 (Figure 3a—the simulated Doppler velocity image (plan position indicator (PPI) image at an elevation angle of 1.0 degree with respect to the horizon for HKBCF SRL). Compare this figure with Figure 2a). WRF-FastEddy seems to reproduce the building-

induced turbulence due to the building complex to the south of the runways reasonably well. In the model-simulated TKE map (Figure 3b), turbulent flow is seen downstream of the buildings within the model domain.



(**a**)



(**b**)

Figure 3. FastEddy-simulated Doppler velocity (**a**) and TKE map (**b**).

The simulated Doppler velocity of HKBCF SRL is compared with the actual LIDAR observations in Figure 4a, temporally covering the period of 05:30 UTC to 08:00 UTC (the first half an hour of the simulation time is not included in order to allow spin-up of the model) and spatially including the 80% of the length of the FastEddy model domain (i.e., 10% of the length just immediate to the model boundary is not included in order to avoid boundary effect). The slope of the best-fit linear equation is close to unity, and the correlation coefficient is about 0.6. The root-mean-square difference is about 2 m/s, which is non-trivial relative to the observed wind speed range in this moderate-wind case, yet it remains within the tolerance reported in LES validation studies for comparable conditions. All these values suggest reasonably good reproduction of the observed wind features. In particular, the model reproduces the qualitative flow structures—such as accelerated zones and turbulence behind buildings—which are critical for hazard identification even when quantitative agreement is imperfect. The underestimation observed is likely due to grid resolution constraints and simplifications in turbulence parameterization; no empirical correction factors are proposed, as these may compromise physical consistency. The model-simulated TKE is plotted with the LIDAR-based EDR in Figure 4b in a log–log plot. The TKE in general increases with EDR. This is the first result in the literature about comparison of FastEddy output with LIDAR measurements for an extended period.

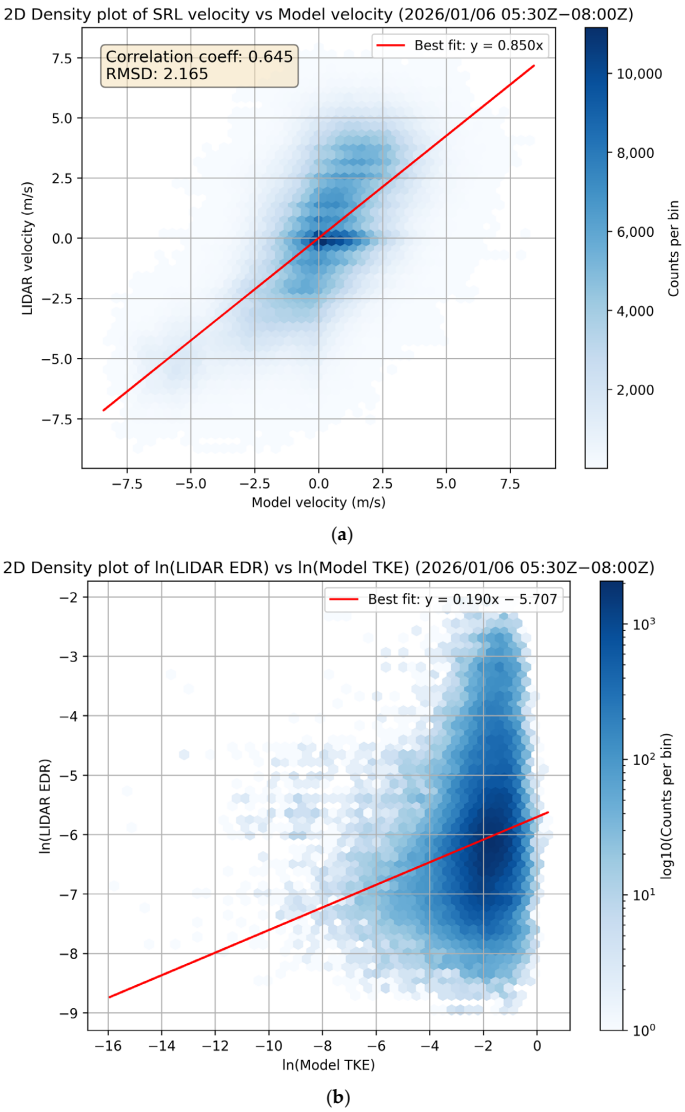
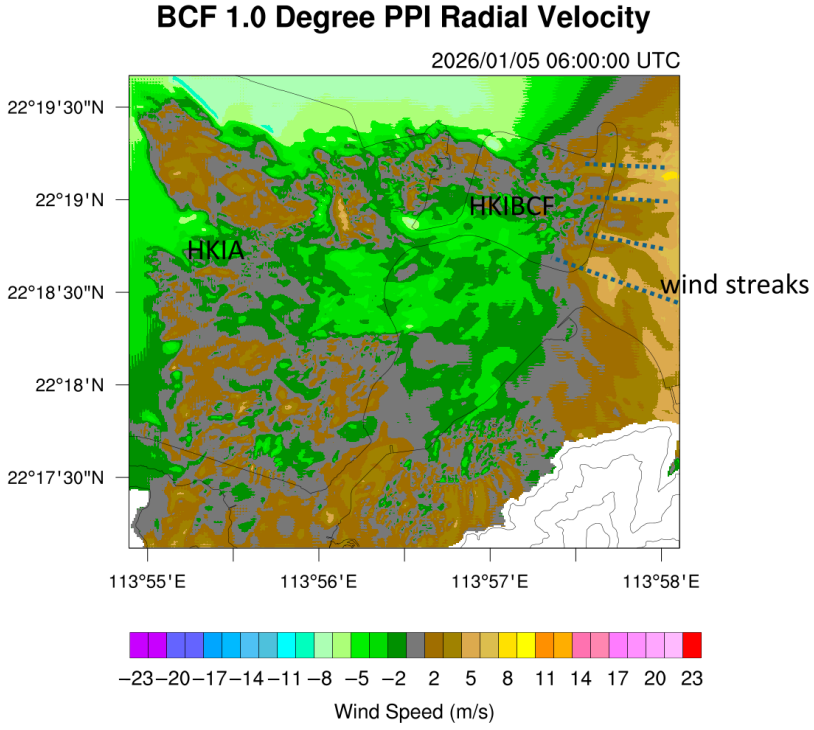


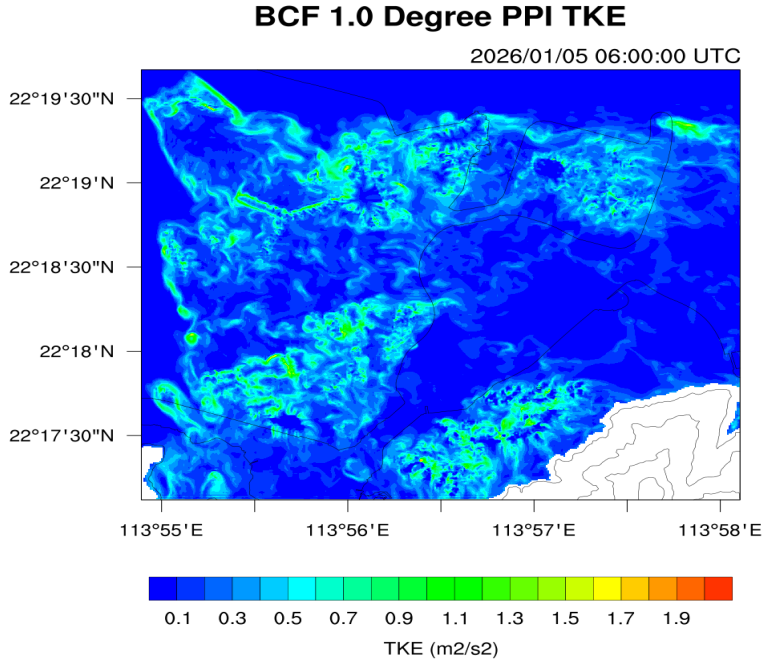
Figure 4. Scatter plots of (**a**) Doppler velocity and (**b**) model TKE with LIDAR EDR.

4. Streaks Downstream of Buildings

In [19], with general northwesterly flow, boundary-layer wind streaks are observed by the HKBCF SRL downstream of the buildings of the HKBCF island. FastEddy simulation is performed starting from 05 UTC on 5 January 2026 and the simulated Doppler velocity image is shown in Figure 5a. Four streaks of outbound wind flow have been successfully simulated, which is similar to the actual observations in [19]. The simulated TKE map (Figure 5b) also shows that the airflow is turbulent over the HKBCF island and downstream of the island due to the effects of the buildings.



(**a**)



(**b**)

Figure 5. FastEddy-simulated Doppler velocity (**a**) and TKE map (**b**) for wind streaks.

To study the effect of the buildings further, a FastEddy simulation was performed without the presence of the buildings, and the simulated Doppler velocity is shown in Figure 6. It could be seen that the airflow is more uniform without the buildings, and the wind streaks extended from the buildings are no longer present. As such, the WRF-FastEddy model again confirms that the observed wind streaks from HKBCF SRL are related to the effects of the buildings on the boundary layer flow.

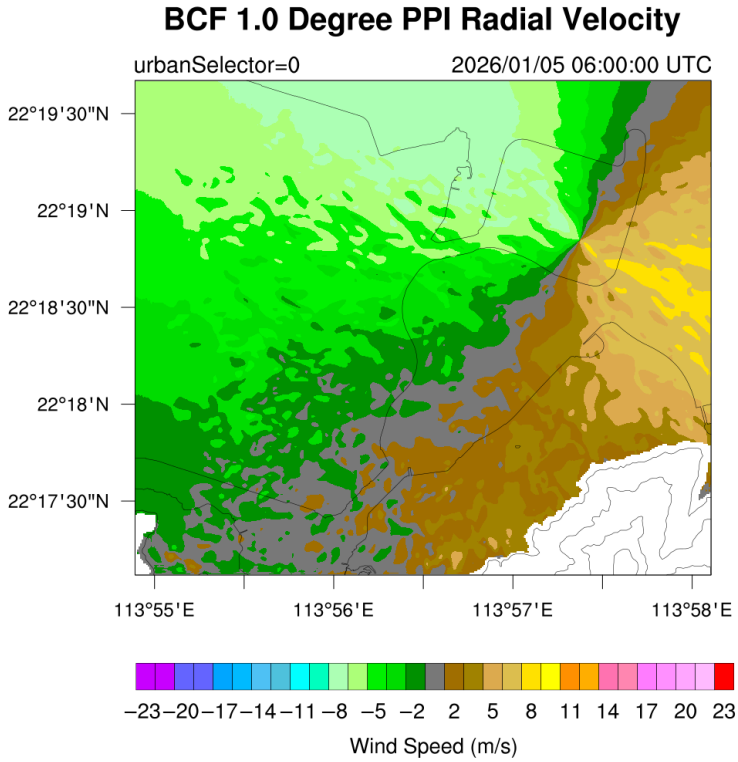
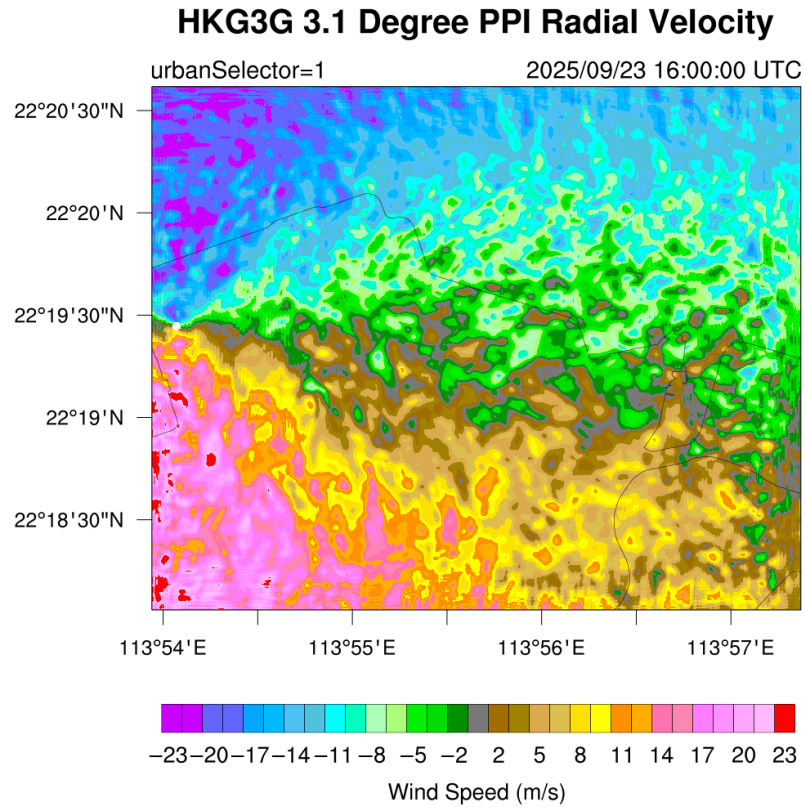


Figure 6. FastEddy-simulated Doppler velocity for the case of wind streaks without the presence of buildings on HKBCF island.

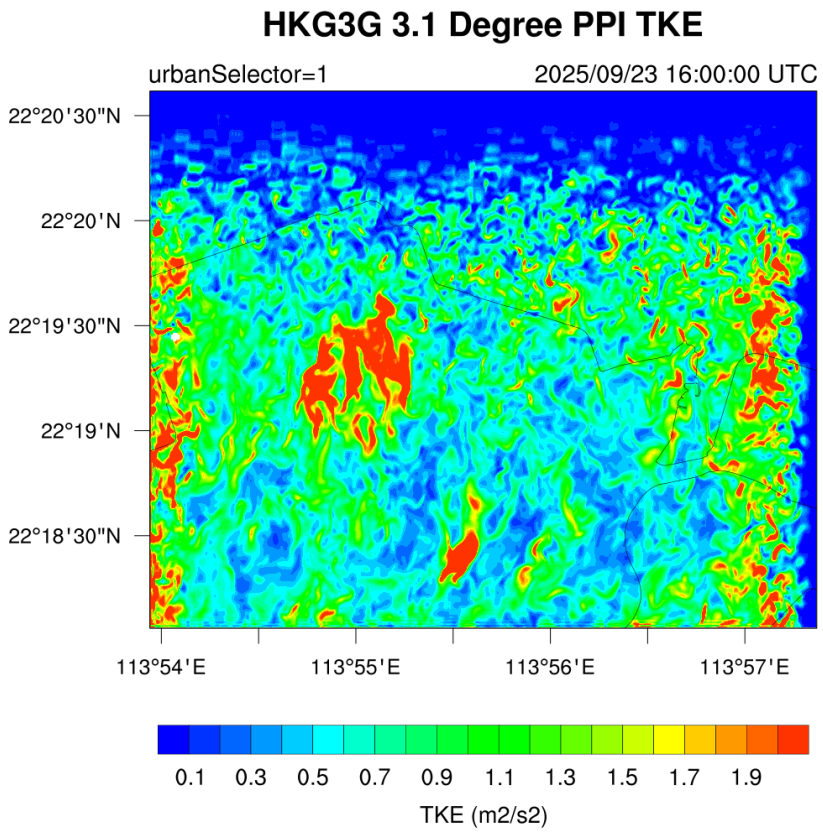
5. Building-Disturbed Airflow in a Typhoon

This is the first time that the WRF-FastEddy coupled model has been tested in a typhoon case, when Hong Kong is under the influence of Super Typhoon Ragasa on 23 to 24 September 2025. The first simulation is initialized at 13 UTC on 23 September 2026. For a three-hour simulation (Figure 7a) with the presence of the buildings inside and around the airport, highly turbulent flow is found in generally northwesterly winds, and model TKE is particularly intense (reaching 2 m2/s2) downstream of the buildings, such as the new terminal building (Figure 7b).

On the following day, the wind direction changes to southeasterly and there is weakening of the winds as Ragasa departs from Hong Kong. FastEddy is initialized at 13 UTC on 24 September 2026, and the other three-hour simulation results are presented here. The model-simulated Doppler velocity image is shown in Figure 8a, again showing turbulent flow over the airport island. TKE remains high downstream of the buildings (Figure 8b), though, compared to Figure 7b, the spatial extent of the building wake has been reduced with the weakening of the winds.

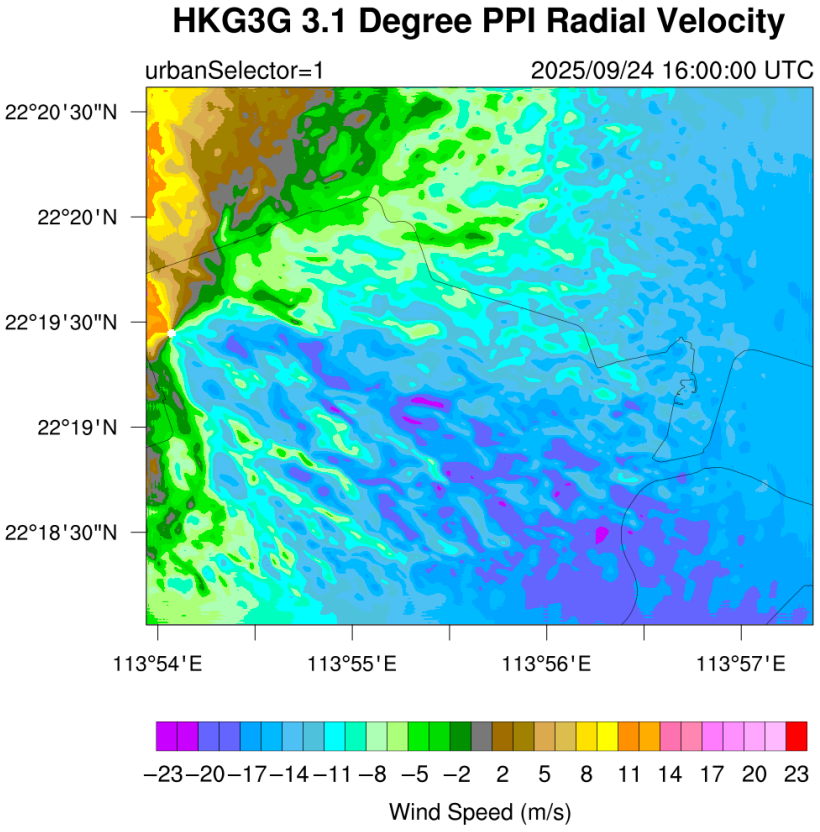


(**a**)

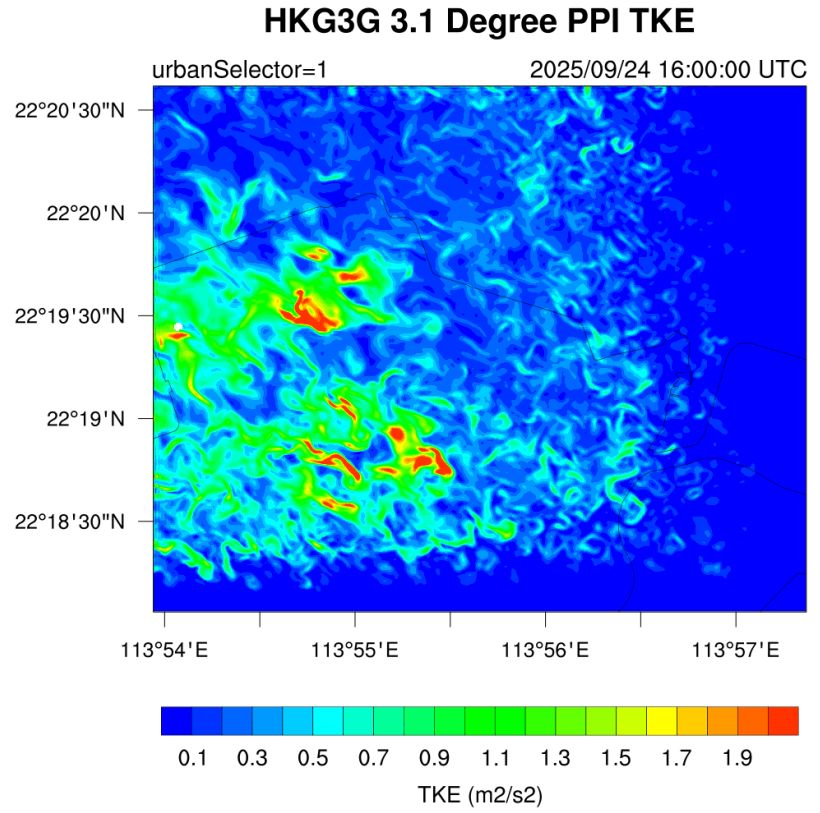


(**b**)

Figure 7. FastEddy-simulated Doppler velocity (**a**) and TKE (**b**) on 23 September 2025.



(**a**)



(**b**)

Figure 8. FastEddy-simulated Doppler velocity (**a**) and TKE (**b**) for 24 September 2025.

The simulated Doppler velocities are compared with the SRL-observed winds, namely, between 15:30 UTC and 18:00 UTC on 23 September 2025 in Figure 9a, and between 14:30 UTC and 17:00 UTC on 24 September 2025 in Figure 10a. The slopes of the best-fit linear equations are in the region of 0.7 to 0.9. The correlation coefficients are between 0.6 and 0.9. The root-mean-square difference is about 4 m/s. Although 4 m/s RSMD represents a noticeable deviation compared with the observation wind speed, they are still consistent with the acceptable range documented in LES validation studies for high-wind environments. All these metrics suggest that the simulation results are generally satisfactory. The observed underestimation likely reflects the limits of grid resolution and the simplifications inherent in the turbulence parameterization. No empirical correction factors are introduced, in order to preserve physical consistency. The model-simulated TKE is compared with the LIDAR-measured EDR in Figures 9b and 10b. In general, TKE is increasing with EDR, and the slopes and y-intercepts are similar in order of magnitude to the northwesterly wind case in Figure 4b. As such, for a super typhoon case and turbulent flow associated with buildings in such atmospheric conditions, the WRF-FastEddy coupled model appears to give reasonable results in comparison with actual LIDAR observations.

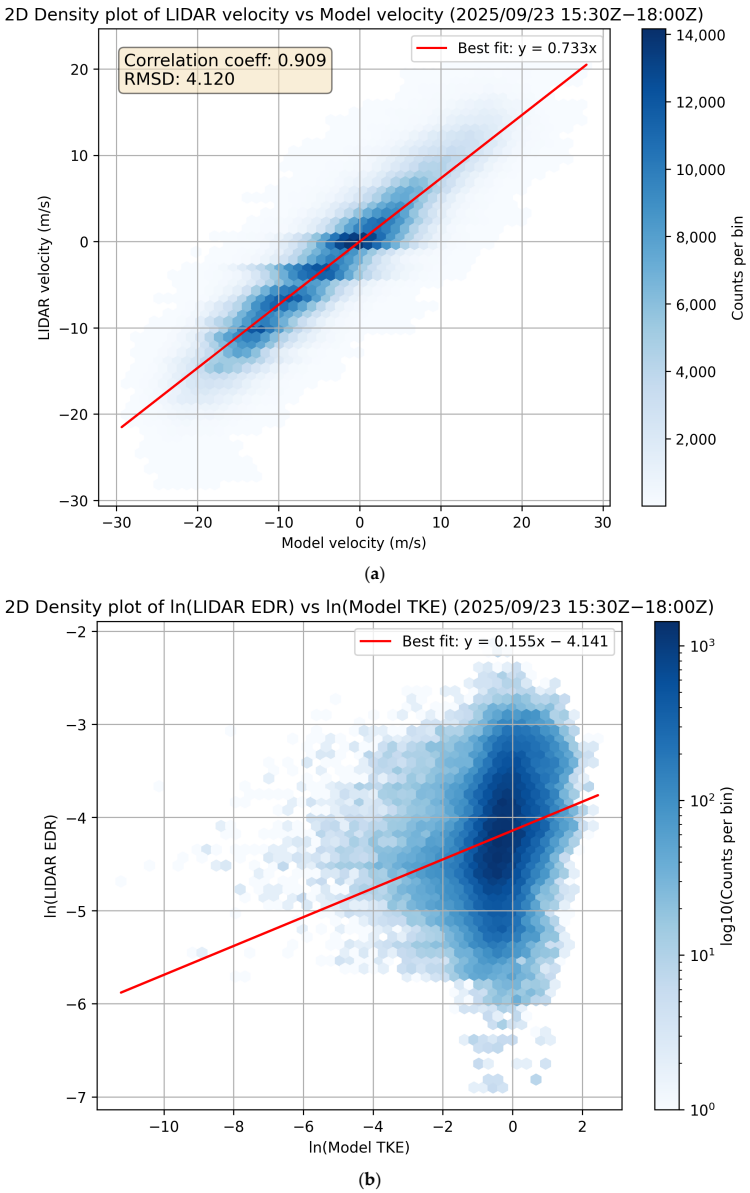


Figure 9. Scatter plot of Doppler velocity (**a**) and TKE-EDR (**b**) for 23 September 2025.

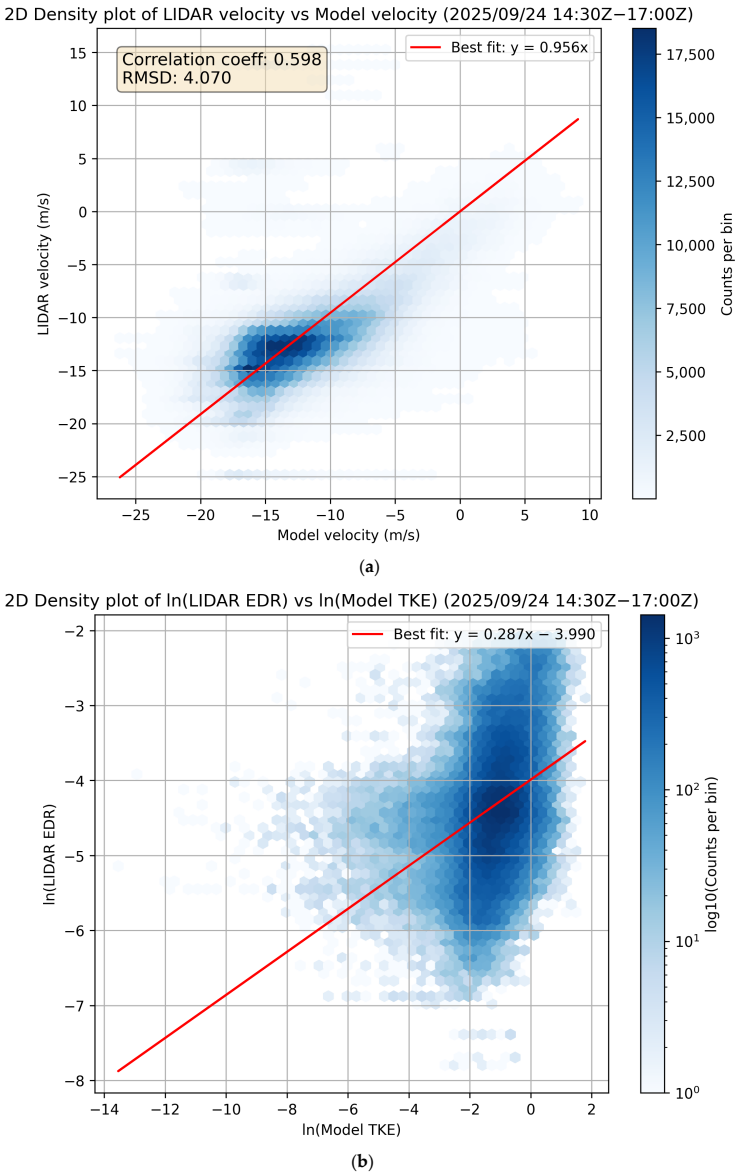
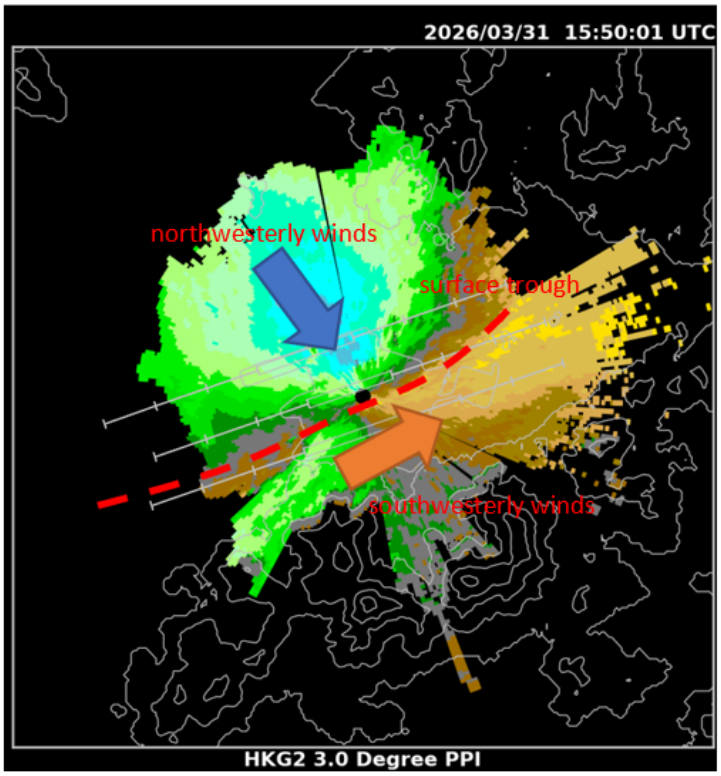


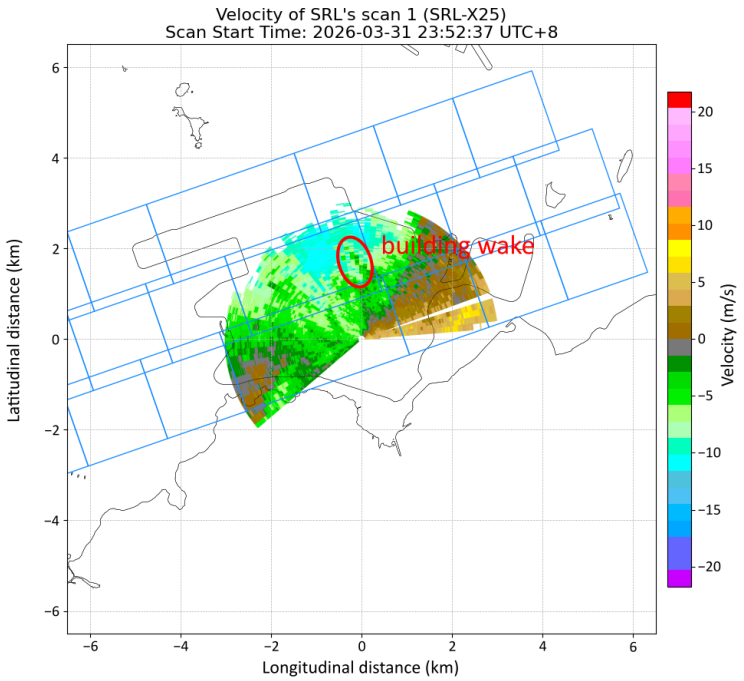
Figure 10. Scatter plot of Doppler velocity (**a**) and TKE-EDR (**b**) for 24 September 2025.

6. Building-Induced Buffeting of an Aircraft

This case is an actual case of low-level wind effect as experienced by the pilot of an arriving aircraft. At about 15:50 UTC on 31 March 2026, a surface trough of low pressure was crossing the western part of Hong Kong. There is convergence between the southwesterly flow ahead of the trough and the northwesterly flow behind the trough, as shown in the Doppler velocity imagery from a long-range LIDAR at the center of the middle runway of HKIA (Figure 11a). For an SRL at the southern runway (the so-called X25 SRL), disturbed flow appears in the generally northwesterly flow (Figure 11b), and such disturbed flow appears to be related to the new terminal building under construction at the airport. The EDR map from this SRL also shows an extended region of higher turbulence downstream of this building (Figure 12a).



(**a**)

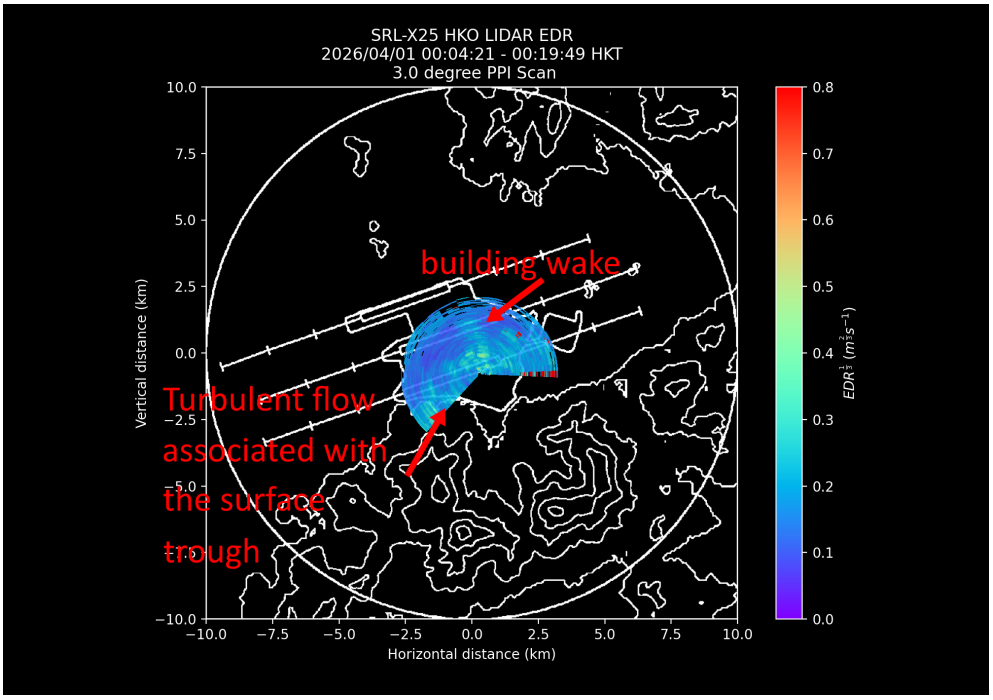


(**b**)

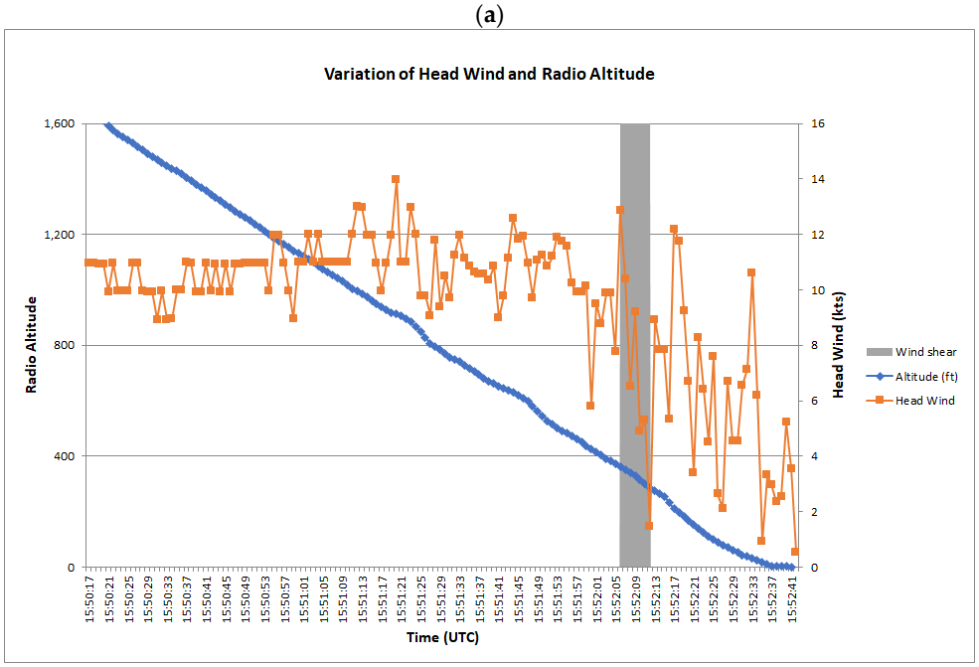
Figure 11. SRL (X25) PPI 3.0 degree Doppler velocity of LIDAR showing arrival of northwesterly (**a**) and SRL Doppler velocity showing turbulent flow from the new terminal building (**b**).

At this time, an aircraft arrived at the middle runway of HKIA from the east, i.e., the 25CA runway corridor. The pilot of that aircraft reported the experience of some degree of buffeting during the landing. From the headwind profile of the aircraft from Quick Access

Recorder (Figure 12b), there were several instances of quite significant fluctuations shortly before landing, with headwind change of a few knots each time. From the crosswind profile (Figure 12c), although the mean crosswind has not reached 25 knots, the crosswind changes do reach 7 knots two times, a gain from around 0 knots to 20 knots at first, which may be related to the entering of the boundary layer northwesterly flow associated with the surface trough of low pressure and is synoptic in scale, and from around 18 knots to 3 knots near touchdown, which is the subject of the present investigation and may be related to the low-level wind effect of the new terminal building.

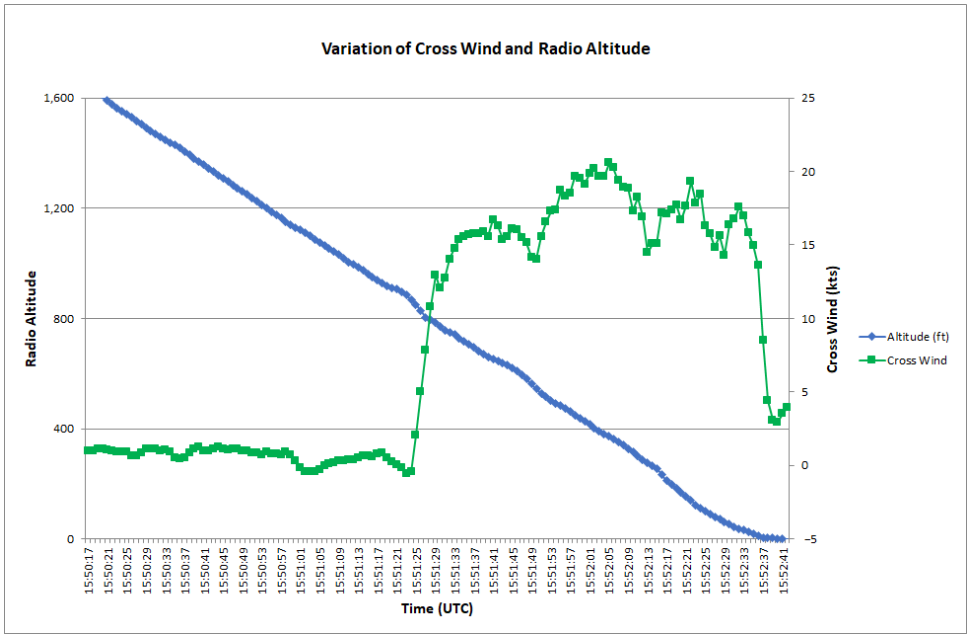


(**a**)



(**b**)

Figure 12. *Cont.*



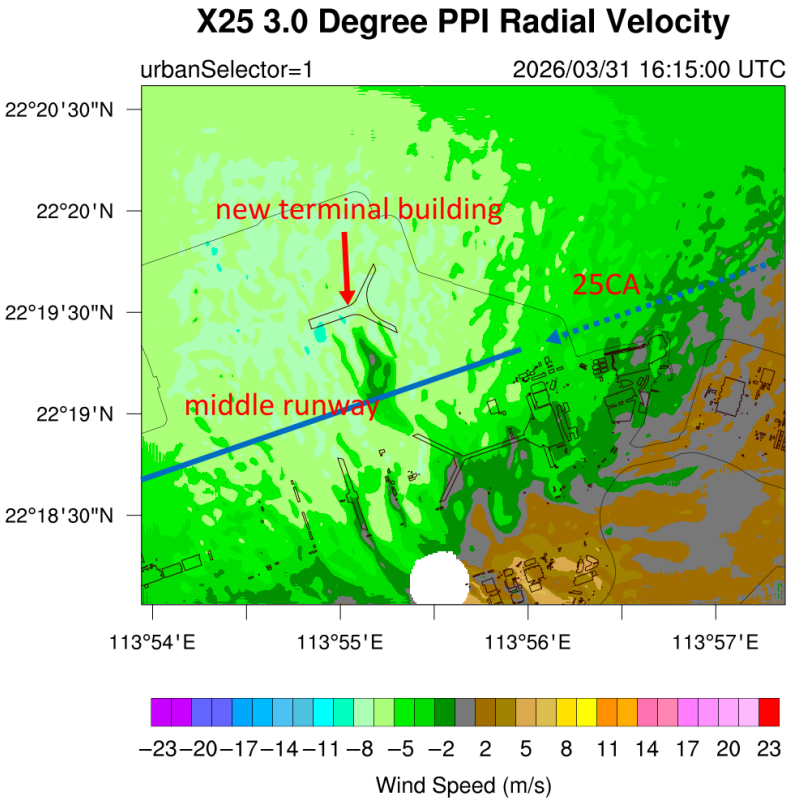
(**c**)

Figure 12. EDR map from SRL (**a**); headwind (**b**) and crosswind (**c**) profiles from aircraft.

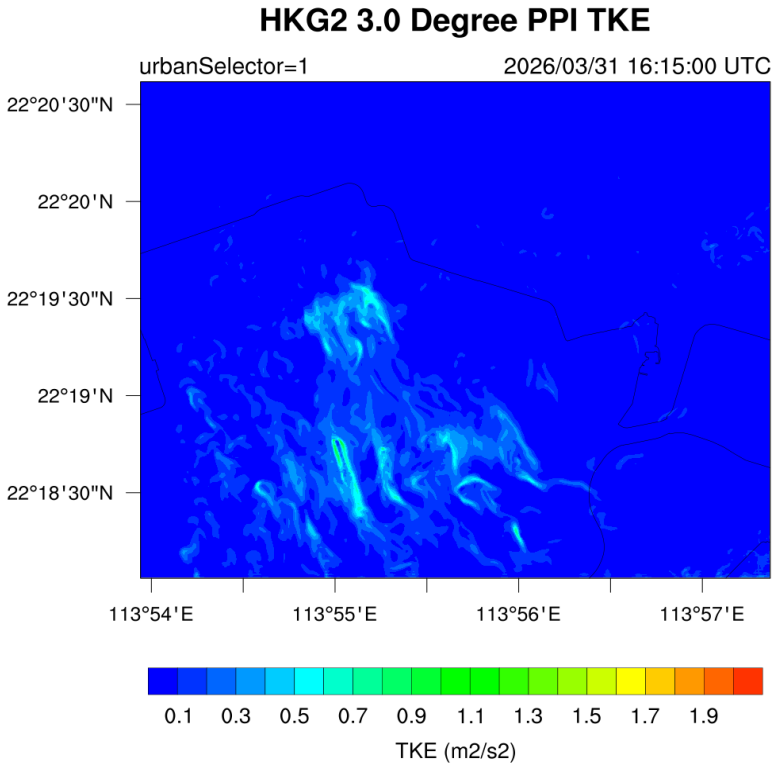
To understand the low-level wind effect, a FastEddy simulation was performed with the presence of all buildings, and the simulated Doppler velocity imagery from X25 SRL is shown in Figure 13a, together with the TKE map in Figure 13b. The location of the new terminal building is also shown in Figure 13a. The surface trough reaches the airport slightly later in the simulation as compared with the actual observation, namely, at about 16:15 UTC on 31 March 2026, and reverse flow with low-level turbulence has been successfully simulated downstream of the new terminal building. The simulated headwind, crosswind and TKE profiles of 25CA glide path are shown in Figures 14a, 14b and 14c respectively. Figure 14d,e further compare the aircraft-observed headwind and crosswind profiles with the corresponding FastEddy simulations at the same time. Arising from the new terminal building, the simulated headwind shows some fluctuations, with headwind change of about 10 knots. The crosswind has two significant changes, namely, the first rise from about 3 knots to 10 knots at about 1–2 nautical miles from the runway end, which is synoptic in scale, and down to around 3 knots again near touchdown, which is related to the terminal building. The TKE increases sharply just before reaching the threshold, and the increase is before the crosswind drop due to the new terminal building. It is not certain whether the increase in TKE is solely related to the wake of the building or the surface mixing associated with the arrival of the northwesterly winds behind the trough of low pressure.

An identical set of simulations has also been performed without the presence of the new terminal building. From the simulated PPI scan of SRL, the winds are more uniform over the touchdown zone of 25CA at the time of the event (16:15 UTC, Figure 15a). Higher TKE is generally associated with the strengthening of the northwesterly winds behind the trough of low pressure (Figure 15b). By comparing the results of Figures 13 and 15, the new terminal building is found to produce a significant building wake with turbulent flow. Without the terminal building, the significant changes of the headwind and crosswind in the touchdown area of 25CA are no longer present in the simulation results (Figure 16a,b). The major crosswind change is associated with the arrival of the northwesterly flow behind the surface trough of low pressure. On the other hand, significant TKE is still observed from 0.2 nautical miles before the touchdown zone of 25CA even in the absence of the new terminal building in the simulation (Figure 16c). The turbulence appears to be more related

to the arrival of the northwesterly winds behind the surface trough of low pressure, and partly related to the wake of the new terminal building.

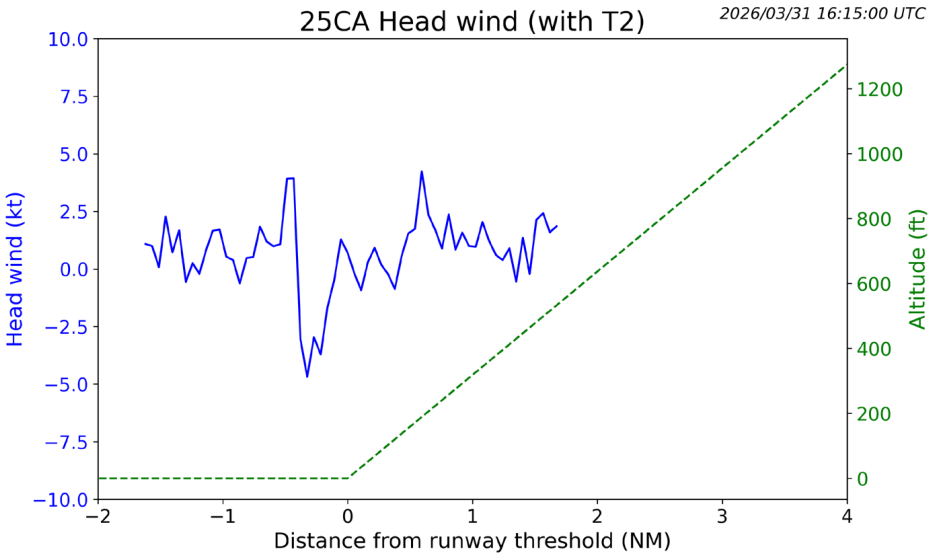


(**a**)

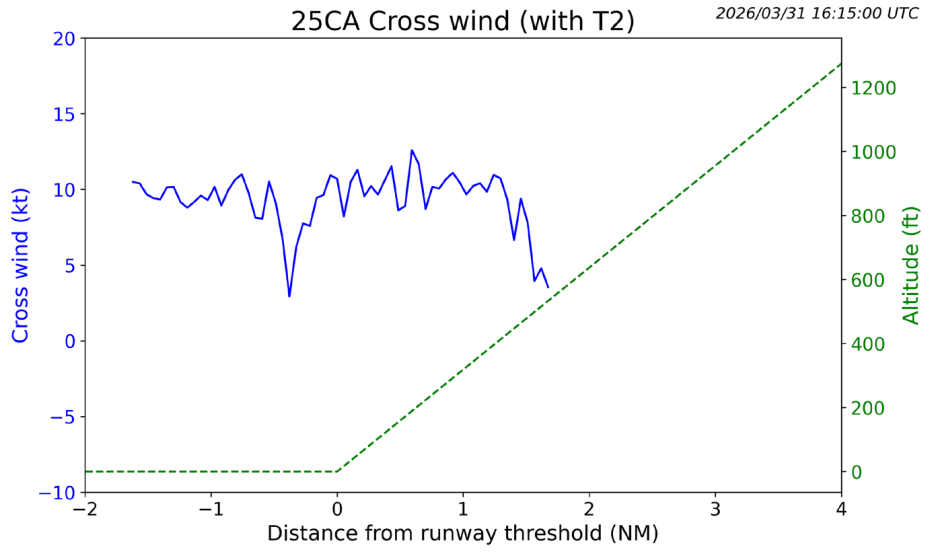


(**b**)

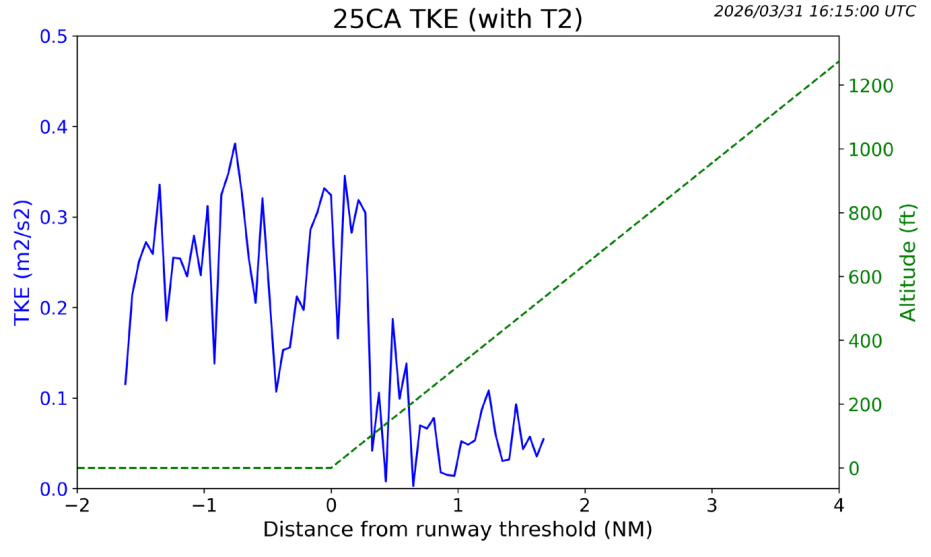
Figure 13. FastEddy-simulated Doppler velocity (**a**) and TKE (**b**) for low-level wind effect case.



(**a**)

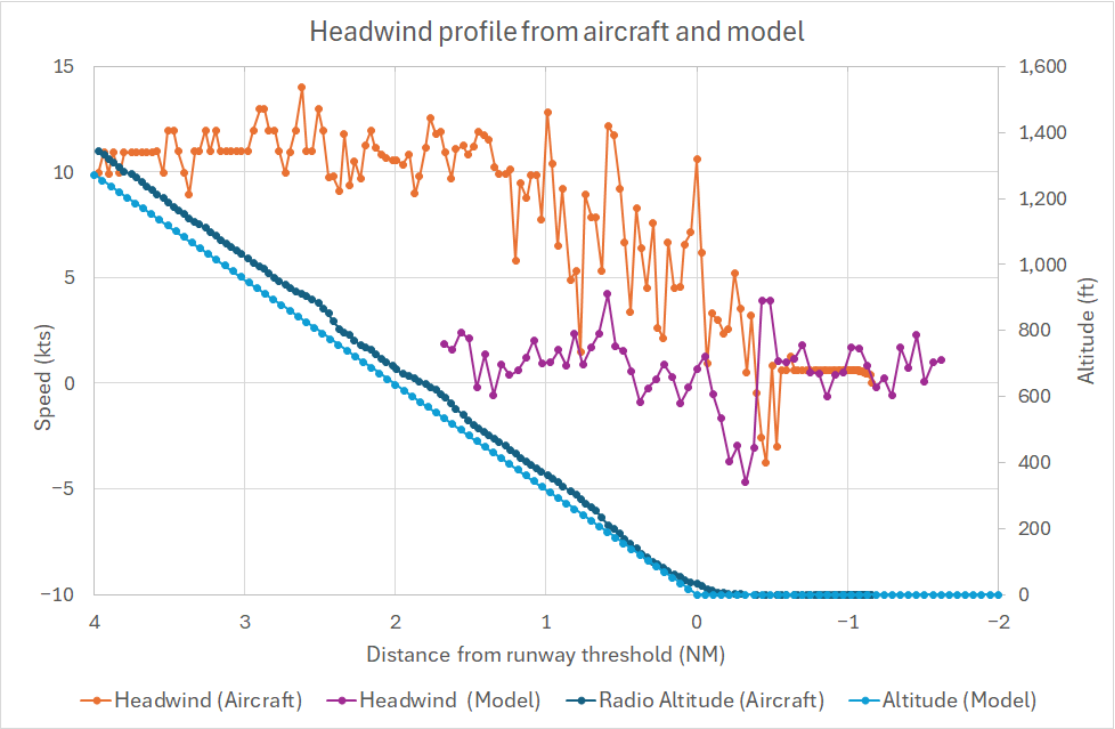


(**b**)

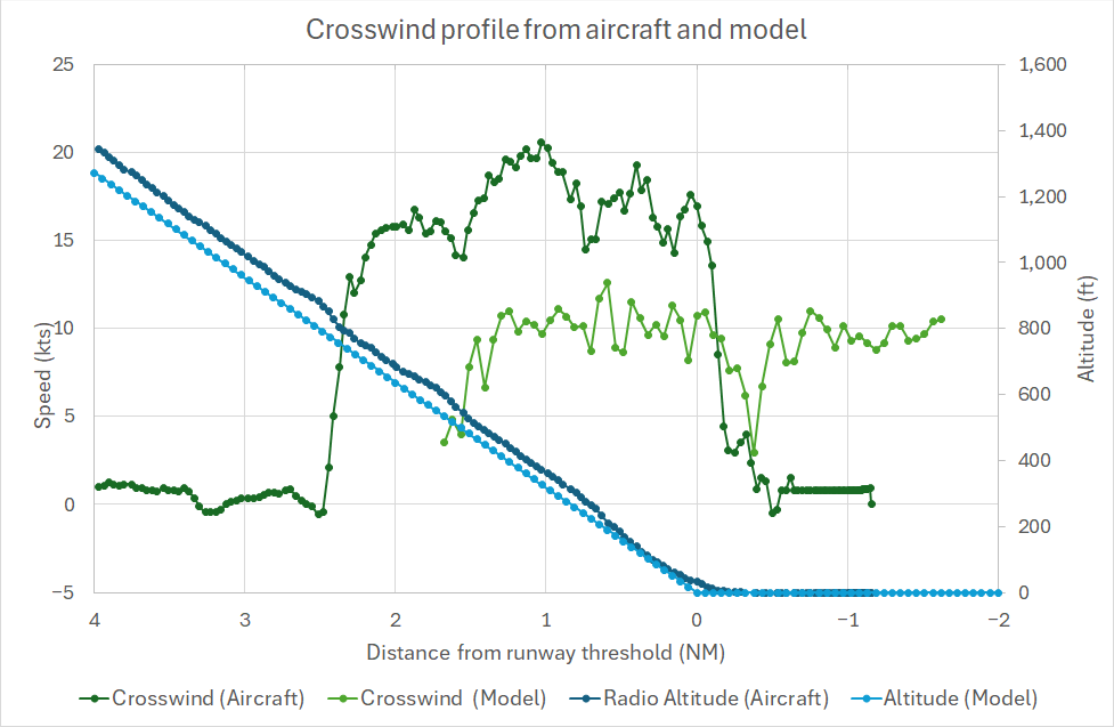


(**c**)

Figure 14. *Cont.*

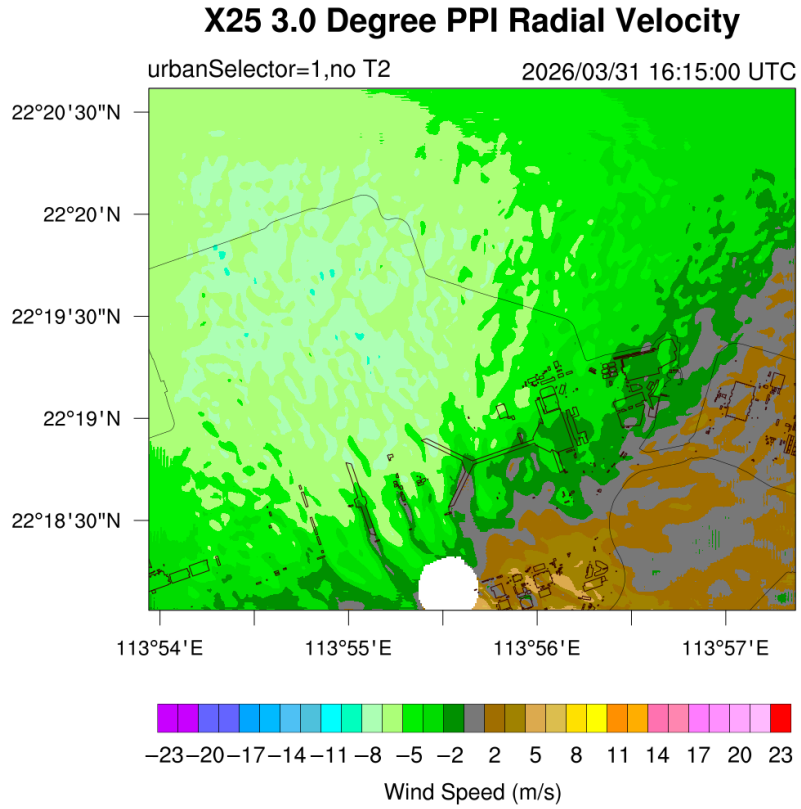


(**d**)

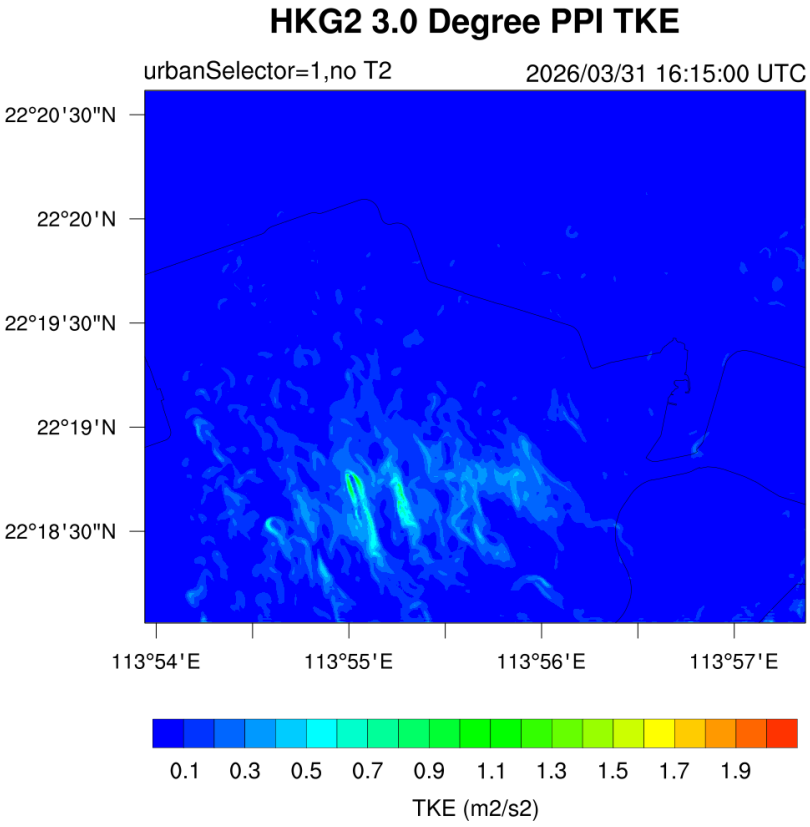


(**e**)

Figure 14. FastEddy-simulated profiles for headwind (**a**), crosswind (**b**) and TKE (**c**) for 25CA glide path at 16:15 UTC on 31 March 2026. Aircraft observations compared with FastEddy simulations for headwind (**d**) and crosswind (**e**) at the same time.

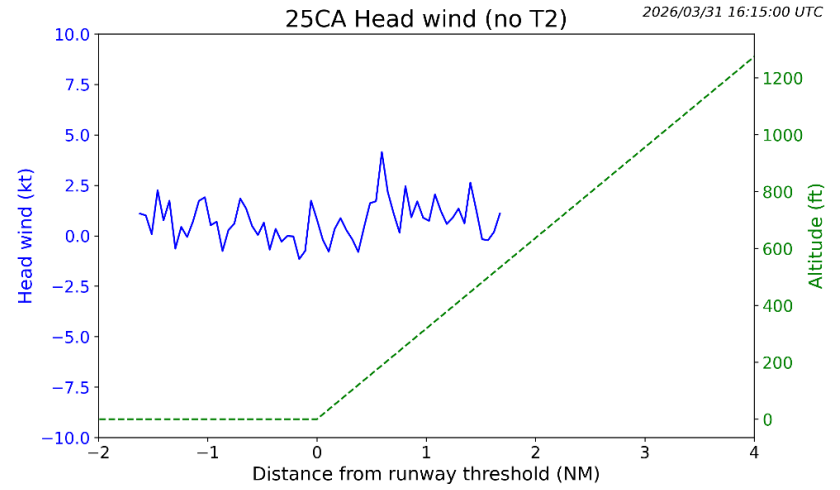


(**a**)

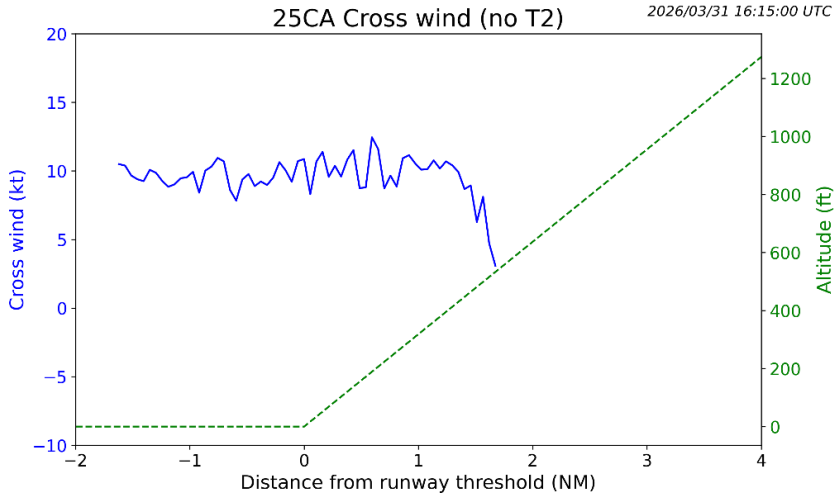


(**b**)

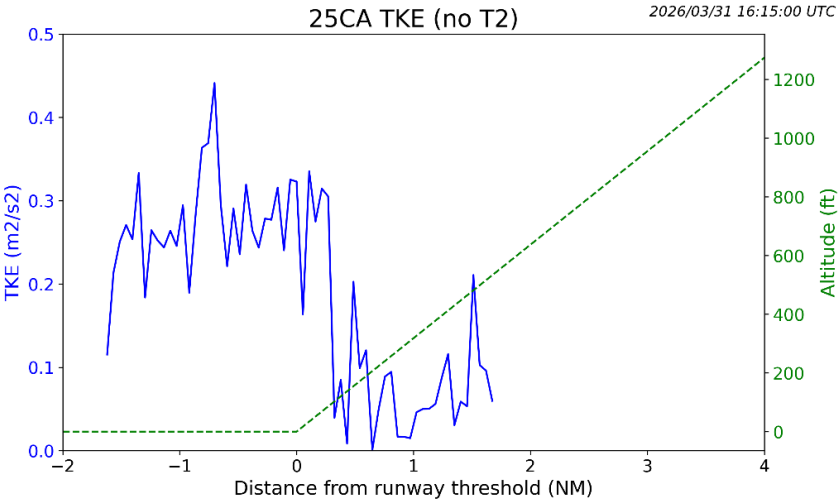
Figure 15. FastEddy-simulated Doppler velocity (**a**) and TKE (**b**) for low-level wind effect case, without the new terminal building.



(**a**)

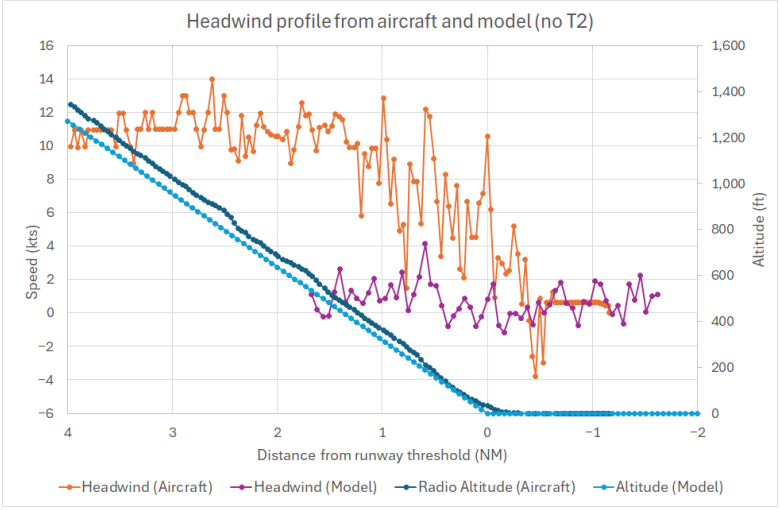


(**b**)

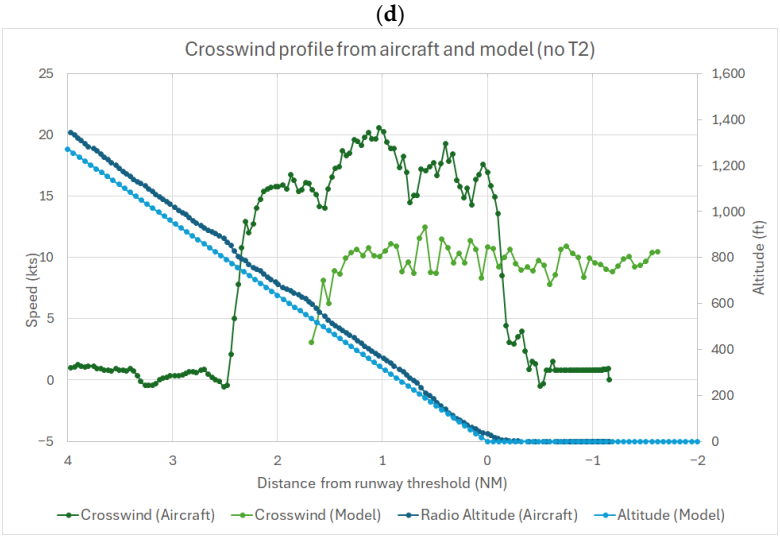


(**c**)

Figure 16. *Cont.*



(**d**)



(**e**)

Figure 16. FastEddy-simulated profiles for headwind (**a**), crosswind (**b**) and TKE (**c**) for 25CA glide path at 16:15 UTC onf 31 March 2026, without the new terminal building. Aircraft observations compared with FastEddy simulations for headwind (**d**) and crosswind (**e**) at the same time.

7. Conclusions

This paper is the first of its kind to study the performance of the WRF-FastEddy coupled model in an operating airport by comparing with LIDAR and aircraft data. A number of novel applications have been discussed, namely, the building-induced turbulent flow in a super typhoon case, and an actual case of low-level wind effect following the arrival of a surface trough of low pressure. Quantitative comparison with LIDAR observations has been made for selected cases, namely, for Doppler velocity and TKE-EDR comparison. In general, the WRF-FastEddy simulation results are reasonable, and they are consistent with the LIDAR observations, aircraft data and pilot experience. With GPU implementation, this coupled model demonstrates, for the first time, the applicability of a GPU-based LES framework to a complex environment under extreme meteorological conditions, with the potential for near real-time forecasting and timely alerts of low-level wind effects from buildings and other human-made structures in an operating airport. Importantly, this study highlights the operational relevance of FastEddy, showing how LES simulations can complement HKIA's existing sensor-based wind shear alert system by providing predictive guidance on turbulence zones associated with new structures or evolving synoptic disturbances.

It is noted that the present paper considers four case studies only. The number of buildings considered in each case is also rather limited. This study could be extended through comparison

with ground-based anemometer readings. Moreover, complex environments in urban areas, such as the downtown area of Hong Kong, in typhoon cases should also be considered. More tests could be conducted to find out the capability and limitations of this coupled model in different setups of buildings. Specifically, the current horizontal (15 m) and vertical (67 m) resolution may under-resolve sharp-edge vortices, potentially underestimating peak turbulence. Moreover, instead of relying on TKE substitution, future work will attempt direct EDR output from the prognostic TKE equation in FastEddy, allowing sub-grid-scale EDR to be compared directly with actual EDR observations (e.g., from LIDARs). This will reduce uncertainty for aviation applications and allow assessment of whether FastEddy can meet operational requirements. In addition, stable stratification was not explicitly tested in this study; future work will evaluate FastEddy under nocturnal inversion conditions, which are relevant for wind shear hazards at airports and consistent with known upper limits of wind shear in stably stratified flows [20]. Together, these extensions will help evaluate whether FastEddy can meet operational aviation requirements and complement existing sensor-based wind shear alert systems.

Author Contributions: Conceptualization, M.L.C. and P.W.C.; methodology, M.L.C. and P.W.C.; software, M.L.C. and K.K.L.; validation, M.L.C. and P.W.C.; formal analysis, M.L.C.; investigation, M.L.C. and K.K.L.; resources, P.W.C.; data curation, M.L.C. and K.K.L.; writing—original draft preparation, P.W.C.; writing—review and editing, M.L.C. and K.K.L.; visualization, M.L.C. and K.K.L.; supervision, M.L.C. and P.W.C.; project administration, P.W.C. All authors have read and agreed to the published version of the manuscript.

Funding: This research received no external funding.

Data Availability Statement: The data presented in this study are available on request from the corresponding author due to privacy concerns.

Conflicts of Interest: The authors declare no conflicts of interest.

Appendix A

Table A1. Parameterization settings table.

Parameter	Value	Meaning
Nx	392	elements in the x direction
Ny	314	elements in the y direction
Nz	58	elements in the z direction
d_xi	15	resolution in the “i” direction
d_eta	15	resolution in the “j” direction
d_zeta	67	resolution in the “k” direction
dt	0.03125	timestep resolution in seconds
verticalDeformFactor	0.42	deformation factor
verticalDeformQuadCoeff	0	deformation factor
hydroBCs	1	Dirichlet lateral ceiling and surface boundary conditions
ceilingAdvectionBC	1	non-zero w-BC
advectionSelector	3	hybrid 5th–6th order
moistureSelector	1	on
turbulenceSelector	1	Lilly/Smagorinsky scheme
TKESelector	1	Prognostic TKE
canopySelector	0	Off
diffusionSelector	0	Off

References

1. Hong Kong Observatory. Low Level Wind Effect. 2026. Available online: https://www.hko.gov.hk/en/aviat/amt/cause/lowlevelwindeffect.html (accessed on 1 May 2026).
2. Liu, X.; Zhang, H.; Wu, S.; Wang, Q.; He, Z.; Zhang, J.; Li, R.; Liu, S.; Zhang, X. Effects of buildings on wind shear at the airport: Field measurement by coherent Doppler lidar. *J. Wind Eng. Ind. Aerodyn.* **2022**, *230*, 105194. [CrossRef]
3. Malin, B. Assessment of Building-Generated Windshear at Airports. In Proceedings of the 21st Australasian Wind Engineering Society Workshop. Airborne Wind Energy Systems (AWES), Sydney, Australia, 2–3 February 2023. Available online: https://awes.org/wp-content/uploads/2024/10/Paper-023-Ben-Malin.pdf (accessed on 1 May 2026).
4. Wang, S.; De Roo, F.; Thobois, L.; Reuder, J. Characterization of Terrain-Induced Turbulence by Large-Eddy Simulation for Air Safety Considerations in Airport Siting. *Atmosphere* **2022**, *13*, 952. [CrossRef]
5. Nieuwpoort, A.M.H.; Gooden, J.H.M.; de Prins, J.L. *Wind Criteria Due to Obstacles at and Around Airports*; Report No. NLR-TP-2010-312; National Aerospace Laboratory NLR: Amsterdam, The Netherlands, 2010. Available online: https://reports.nlr.nl/server/api/core/bitstreams/7785644b-929f-46ae-ba44-1259969da89d/content (accessed on 1 May 2026).
6. Krüs, H.W.; Haanstra, J.O.; van der Ham, R.; Schreur, B. Numerical simulations of wind measurements at Amsterdam Airport Schiphol. *J. Wind. Eng. Ind. Aerodyn.* **2003**, *91*, 1215–1223. [CrossRef]
7. Knigge, C.; Raasch, S. Large-Eddy Simulation on the Influence of Buildings on Aircraft During Take off and Landing. Institute of Meteorology and Climatology, Leibniz Universität Hannover. 2014. Available online: https://www.meteo.uni-hannover.de/fileadmin/meteo/publications/Knigge_JGM_2014_LongAbstract_Template.pdf (accessed on 1 May 2026).
8. Lo, K.W.; Hon, K.K.; Chan, P.W.; Li, L.; Li, Q.S. Simulation of building-induced airflow disturbances in complex terrain using meteorological-CFD coupled model. *Meteorol. Z.* **2022**, *31*, 317–330. [CrossRef]
9. Sauer, J.; Muñoz-Esparza, D. The FastEddy resident-GPU accelerated large-eddy simulation framework: Model formulation, dynamical-core validation and performance benchmarks. *J. Adv. Model. Earth Syst.* **2020**, *12*, e2020MS002100. [CrossRef]
10. Shin, H.H.; Muñoz-Esparza, D.; Sauer, J.A.; Steiner, M. Large-Eddy Simulations of Stability-Varying Atmospheric Boundary Layer Flow over Isolated Buildings. *J. Atmos. Sci.* **2021**, *78*, 1487–1501. [CrossRef]
11. Raluy-López, E.; Muñoz-Esparza, D.; Montávez, J.P. A Local Terrain Smoothing Approach for Stabilizing Microscale and High-Resolution Mesoscale Simulations: A Case Study Using FastEddy® (v3.0) and WRF (v4.6.0). *Geosci. Model Dev.* **2026**, *19*, 5139–5154. [CrossRef]
12. Welch, B.M.; Horel, J.D.; Sauer, J.A. Application of the NCAR FastEddy® Microscale Model to a Lake Breeze Front. *Atmosphere* **2024**, *15*, 809. [CrossRef]
13. Smagorinsky, J. General circulation experiments with the primitive equations: I. The basic experiment. *Mon. Weather Rev.* **1963**, *91*, 99–164. [CrossRef]
14. Chan, P.W. Generation of an Eddy Dissipation Rate Map at the Hong Kong International Airport Based on Doppler Lidar Data. *J. Atmos. Ocean. Technol.* **2011**, *28*, 37–49. [CrossRef]
15. Zhu, X.; Qu, Y.; Shi, X. LEX v1.6.0: A New Large-Eddy Simulation Model in JAX with GPU Acceleration and Automatic Differentiation. *Geosci. Model Dev.* **2026**, *19*, 1103–1120. [CrossRef]
16. Bogenschutz, P.A.; Clevenger, T.C.; Bradley, A.M.; Caldwell, P.M.; Beydoun, H.; Mahfouz, N.; Keen, N.D.; Guba, O.; Bertagna, L.; Foucar, J.; et al. High Performance, High Fidelity: A GPU-Accelerated Doubly-Periodic Configuration of the Simple Cloud-Resolving E3SM Atmosphere Model Version 1 (DP-SCREAMv1). *J. Adv. Model. Earth Syst.* **2025**, *17*, e2025MS005127. [CrossRef]
17. Wicker, L.J.; Skamarock, W.C. Time-Splitting Methods for Elastic Models Using Forward Time Schemes. *Mon. Weather Rev.* **2002**, *130*, 2088–2097. [CrossRef]
18. Zanaga, D.; Van De Kerchove, R.; Daems, D.; De Keersmaecker, W.; Brockmann, C.; Kirches, G.; Wevers, J.; Cartus, O.; Santoro, M.; Fritz, S.; et al. *ESA WorldCover 10 m 2021 v200*; ESA WorldCover Consortium: Boeretang, Belgium, 2022. [CrossRef]
19. Lo, K.W.; Cheung, P.; Chan, P.W. Turbulence and wind streaks arising from buildings at the Hong Kong International Airport–observations and numerical simulations. *Urban Clim.* 2026, *submitted*.
20. Emeis, S. Upper Limit for Wind Shear in Stably Stratified Conditions Expressed in Terms of a Bulk Richardson Number. *Meteorol. Z.* **2017**, *26*, 421–430. [CrossRef]

Disclaimer/Publisher's Note: The statements, opinions and data contained in all publications are solely those of the individual author(s) and contributor(s) and not of MDPI and/or the editor(s). MDPI and/or the editor(s) disclaim responsibility for any injury to people or property resulting from any ideas, methods, instructions or products referred to in the content.